


Theoretical studies on internal strain of face-centered-cubic metal nanoparticlesXin Wei  and Da-Jun Shu ^{*}*National Laboratory of Solid State Microstructures, School of Physics, and Collaborative Innovation Center of Advanced Microstructures, Nanjing University, Nanjing 210093, China* (Received 28 March 2022; revised 2 November 2022; accepted 7 November 2022; published 18 November 2022)

Combining the continuum elastic theory and the first-principles calculations, we systematically studied the internal strain of nanoparticles of face-centered-cubic (fcc) metals. By taking full account of the surface anisotropy, the theoretical results are found to be consistent with the previously reported experimental ones within a wide range of nanoparticle sizes. Furthermore, we demonstrate that among the fcc transition metals, the largest internal strain of the nanoparticles with size larger than 5 nm occurs in the last column of the Group VIII (Ni/Pd/Pt), which can be correlated with the filling status of *d*-band electrons of the metals. Most of the fcc metal nanoparticles tend to contract with decreasing size with the only exception of strontium, suggesting that most of the surfaces are dominated by the positive surface stress.

DOI: [10.1103/PhysRevB.106.195419](https://doi.org/10.1103/PhysRevB.106.195419)**I. INTRODUCTION**

The internal strain of nanoparticles is a classic yet still vital topic since it is essential for various properties of the nanoparticles [1,2]. Lattice contraction of metal nanoparticles has been observed by electron reflection [3], electron diffraction [4,5], x-ray adsorption [6], transmission electron microscopy [7], etc. A blueshift of the Mie frequency is usually expected if the lattice parameter diminishes with decreasing particle size [8]. In addition, the *d*-band level positions of transition metals usually shift down with lattice contraction [9], which reduces the surface reactivity of transition metals [10]. It indicates that the increasing negative internal strain with decreasing size of metal nanoparticles is detrimental to chemical catalysis although the large surface-to-volume ratio can provide more reactive sites.

The experimental observations sometimes cannot reveal the intrinsic properties of nanoparticles due to the effect of the supporting substrate [11–13]. Moreover, active metal surfaces are also ready to be oxidized during the preparation process. In this situation, it is actually the surfaces of metal oxides but not the pure metal surfaces that determine the internal strain of the nanoparticles [14]. In contrast, theoretical methods are easy to get rid of effects of substrates or surface oxidation. Based on the continuum elastic theory, a simplified spherical model of metal nanoparticles was previously pursued which suggests that the internal strain is simply proportional to the surface stress over the size of the nanoparticles once the elastic constants are determined [15]. A real metal nanoparticle is certainly not spherical. There are numerous works that introduce the shape factors to consider the orientated anisotropy [16,17]. However, a sufficient description of the anisotropic surface properties is still in short. On the other hand, the internal strain of metal clusters with dozens of atoms has been

directly simulated [18]. Unfortunately, this bottom-up method cannot be scaled up to large nanoparticles due to the limit of the computer capacity. In a word, there is still a lack of work to investigate the intrinsic internal strain of metal nanoparticles in a large size range at the same time, not to mention revealing the relationship between the internal strain of nanoparticles and the electron configurations of the metals.

In this paper, we study the internal strain of nanoparticles of face-centered-cubic (fcc) metals systematically by combining the continuum elastic theory and the first-principles calculations and taking full account of the anisotropy of the surface of nanoparticles [19]. We find the current results are consistent with the previous reports within a wide range of nanoparticle sizes. Furthermore, we demonstrate that the largest internal strain of nanoparticles of fcc transition metals occurs in the last column of Group VIII (Ni/Pd/Pt) if the size is larger than 5 nm. The variation rule of the internal strain with the nanoparticle size is found to be correlated with the filling status of the *d* band of the metals. We also demonstrate that with the exception of strontium, the fcc metal nanoparticles tend to contract with decreasing size, suggesting that most of the surfaces are dominated by the positive surface stress.

II. METHOD AND DETAILS

Since we aim to reveal the correlation between the internal strain of nanoparticles and the electron configurations of the metals, we only focus on one of the typical metal structures, i.e., the fcc phase. As shown in Table I, we investigate totally 17 metals in fcc phases to study the internal strain of their nanoparticles. They can be divided into three blocks according to the orbitals of their valence electrons. Ca, Sr, and Ba are in the *s* block, and Al and Pb are in the *p* block, whereas, Fe/Co/Ni/Cu, Ru/Rh/Pd/Ag, and Os/Ir/Pt/Au are in the *d* block. Actually, in the long periods of the periodic table, the variation of the most stable crystal structures generally

^{*} djshu@nju.edu.cn

TABLE I. The considered 17 fcc metals and their configurations of valence electrons. n means the number of d electrons.

Period	IIA		VIII			IB		IIIA		IVA	
	s		d ($5 < n < 10$)					p			
3								Al ($3s^23p^1$)			
4	Ca ($4s^2$)		Fe ($3d^64s^2$)	Co ($3d^74s^2$)	Ni ($3d^84s^2$)	Cu ($3d^{10}4s^1$)					
5	Sr ($5s^2$)		Ru ($4d^75s^1$)	Rh ($4d^85s^1$)	Pd ($4d^{10}$)	Ag ($4d^{10}5s^1$)					
6	Ba ($6s^2$)		Os ($5d^66s^2$)	Ir ($5d^76s^2$)	Pt ($5d^96s^1$)	Au ($5d^{10}6s^1$)					Pb ($6s^26p^2$)

follows the law of IIB(hcp)-IVB(hcp)-VIB(bcc)-VIIB(bcc)-VIII(hcp/fcc/fcc)-IB(fcc), which is determined primarily by the weight of the d orbitals in the hybrid [20]. The fcc structure is, thus, more common in transition metals with the number of d electrons n larger than 5. It is worthy to mention that the fcc phases of Fe and Co are stable only at temperatures much higher than the room temperature. Besides, fcc phases are not the most stable one at any temperature for Ba, Ru, and Os [21,22]. Even though, we include Ba, Ru, Os, Fe, and Co in order to compare the metals within the same period.

The density functional theory (DFT) calculations are carried out by using the Vienna *ab initio* simulation package code [23–25] with the projector augmented-wave method [26,27] considering the spin polarization. The Perdew-Burke-Ernzerhof (PBE) [28] generalized gradient approximation is employed to describe the electron exchange-correlation energy. The plane-wave energy cutoff of 600 eV is used for expanding the Kohn-Sham wave functions to ensure the accuracy of the surface stress. The surface is modeled by using a slab of eight atomic layers plus a vacuum layer of 15 Å. The structures are fully relaxed until the force on each atom becomes less than 0.01 eV/Å whereas keeping the shape and volume of the slab unchanged. The Γ -centered Monkhorst-Pack k -point meshes of different sizes are used to sample the Brillouin zone of the bulk and the (100), (110), and (111) surfaces of the fcc metals to guarantee the convergence.

For the fcc crystal, the symmetry requires that the off-diagonal elements of the strain tensor are zero, whereas the nonzero diagonal ones are equal to each other, i.e., $\epsilon_{11} = \epsilon_{22} = \epsilon_{33} = \epsilon$. The bulk elastic energy per volume is [29,30]

$$\Delta E_{\text{bulk}}(\epsilon) = \frac{9}{2}B_0\epsilon^2. \quad (1)$$

Meantime, the change in surface energy of each surface of the nanoparticle can be written as [31]

$$\Delta\gamma(\epsilon) = \sigma_0\epsilon + \frac{1}{2}S_0\epsilon^2. \quad (2)$$

Here B_0 is the bulk modulus, $\sigma_0 = \sigma_{11} + \sigma_{22}$ and $S_0 = S_{11} + S_{22} + 2S_{12}$ with σ and S being the surface stress and surface elastic constant, respectively, and the subscripts 1 and 2 being the two in-plane perpendicular directions of the surface. B_0 , σ_0 , and S_0 can be obtained from the DFT calculations by fitting ΔE_{bulk} and $\Delta\gamma$ with strain according to Eqs. (1) and (2), respectively. In the calculation of the surface stress, both unrelaxed surfaces and relaxed ones are considered for comparison. Note that by relaxed surfaces we refer to the surfaces that are relaxed in the atomic coordinates but not relaxed in strain.

Note that the change in the total energy of a nanoparticle with volume V_0 under a certain strain is $\Delta E_{\text{total}} = \Delta E_{\text{bulk}}(\epsilon)V_0 + \sum_i n_i A_i \Delta\gamma_i(\epsilon)$. By minimizing ΔE_{total} with

respect to ϵ , one can obtain the internal strain ϵ of the nanoparticle,

$$\epsilon = -\frac{\sum_i n_i A_i \sigma_{0i}}{9B_0 V_0 + \sum_i n_i A_i S_{0i}}. \quad (3)$$

Here the subscript i is used to distinguish the differently indexed crystal faces. A_i denotes the area of each exposed i th surface, and n_i is the number of the i th surface (see more details in Appendix A).

III. RESULTS AND DISCUSSION

First of all, we need to find out the area of each exposed crystal face of a nanoparticle in equilibrium. The morphology of a nanoparticle is determined by the condition of minimizing the total surface energy under the constraint of a fixed bulk volume V_0 . According to the Wulff rule [32,33], the distance h_i from the geometric center of the nanoparticle to the i th surface is proportional to the surface energy γ_i , i.e., $\frac{\gamma_i}{h_i} = \text{const}$. By this means, the thermally stable morphology of the metal nanoparticles can be obtained with the orientation-dependent surface energies.

Usually only the low index surfaces are exposed due to their low surface energies. Here we consider the (111), (100), and (110) surfaces for all the fcc metals, and their surface energies are shown in Appendix B (Fig. 6). According to the results, we found that the exposed facet number of the nanoparticles are 26 and 14 for metals with small and large atomic numbers, respectively, as shown in blue and red in the insets of Fig. 1. It suggests that the surface anisotropy of the considered metals generally increases with increasing atomic number. The 14-facet gold nanoparticle was adopted theoretically [34] and was observed experimentally [35], which means that by considering the three low index surfaces the surface anisotropy of the metals has been sufficiently accounted for.

As the internal strain depends on the elastic properties, we further calculate the bulk modulus as well as the surface stress and surface elastic constants of (111), (100), and (110) surfaces of all involved metals. The results are shown in Appendices C and D (Figs. 7–9). Based on the equilibrium morphology of a specific metal, the internal strain depending on the nanoparticle size can be obtained according to Eq. (3) by using the obtained bulk and surface elastic properties. The internal strain of all the fcc metal nanoparticles with different sizes is shown in Fig. 1. One can see that the magnitude of the internal strain of Au or Pt nanoparticles can reach 2.5% when the sizes are about 3 nm, whereas it is less than 0.5% for the nanoparticles with the size of 10 nm.

Before further discussing the general rule of the findings for the fcc metals, we need to verify our models by selecting

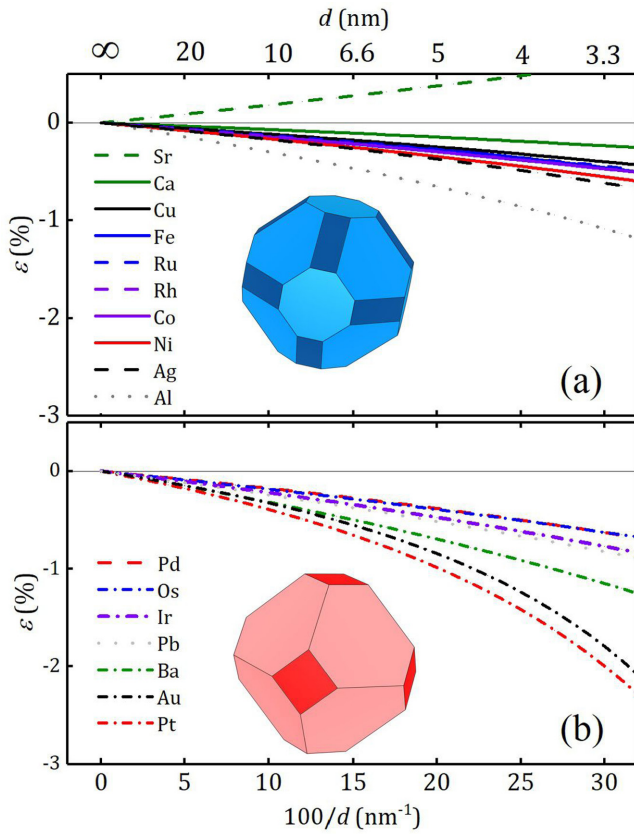


FIG. 1. The variation of the internal strain with the size of the fcc metal nanoparticles. Metals with 26 facets and 14 facets are shown in (a) and (b), respectively.

typical metals to compare the current results with the previously reported ones. The data are collected from the literature for metals Al [13,36,37], Cu [5,6], Pd [7], Ag [4,36,38], Pt [5], and Au [3,39]. As shown in Fig. 2, the data in the literature are divergent from each other so that it is impossible for any theoretical model to be consistent with all the data. Even so, our results are consistent with data from specific sources within a wide range of the nanoparticle size, especially for Al and Cu. It demonstrates that our theoretical models are reliable.

We stress that there is a crossover from noncrystalline to crystalline at very low size. Such crossover generally happens to metals less than 3 nm, e.g., Co [40], Pd, Pt, Au [41], and Rh [42]. For Ag and Cu, the crossover occurs at a larger diameter of about 5 nm [41]. Fortunately, as shown in Fig. 2(a) for Al and Fig. 2(b) for Cu, by fully considering the anisotropy of nanoparticles our theoretical results are roughly consistent with the previously reported data even at size smaller than 5 nm.

Now back to the general rule of the fcc metals. One of the findings in Fig. 1 is that the largest internal strain of the fcc transition metals is always in the last column of the Group VIII (Ni/Pd/Pt) when the size is greater than 5 nm. To visualize it more clearly, the internal strain of $d_1 = 10$ nm and $d_2 = 5$ nm of d -band metal nanoparticles in this paper is shown in Fig. 3. Ni/Pd/Pt obviously lie on the lowest sites in each section of the lines.

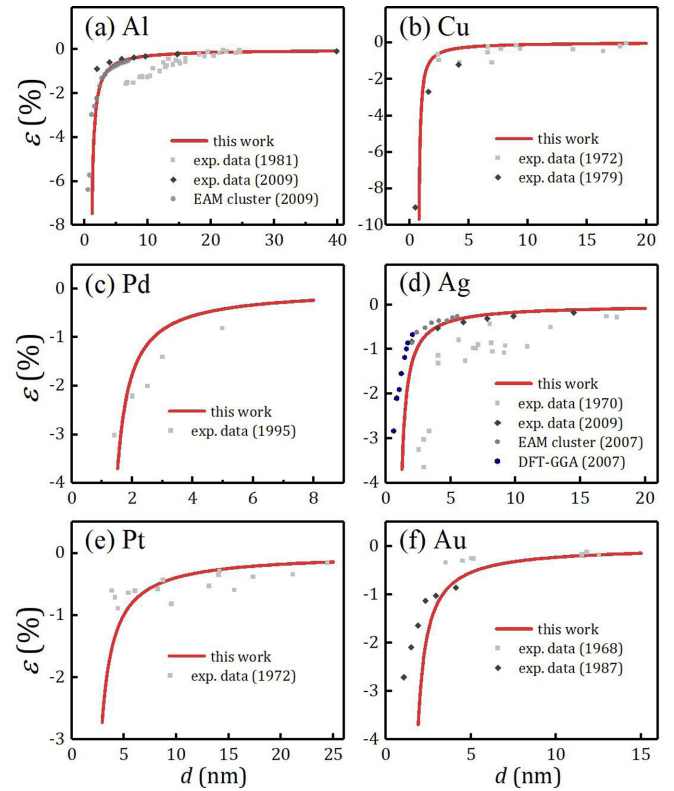


FIG. 2. Comparison of the current paper with the previous reported ones for six typical kinds of fcc metal nanoparticles.

In order to explain why metals in the last column of Group VIII have the largest internal strain among the fcc transition metals, we approximate Eq. (3) by ignoring the surface anisotropy and only include the contribution of the (111) surface due to its lowest surface energy. Moreover, the quadratic term contributed by S_0 can be omitted for nanoparticles with diameters larger than 5 nm. Under these assumptions, we can use the ratio of surface stress σ_0 of the (111) surface to the bulk modulus B_0 to measure the internal strain of a nanoparticle with size of d ,

$$\varepsilon d \propto -\frac{\sigma_0(111)}{B_0}. \quad (4)$$

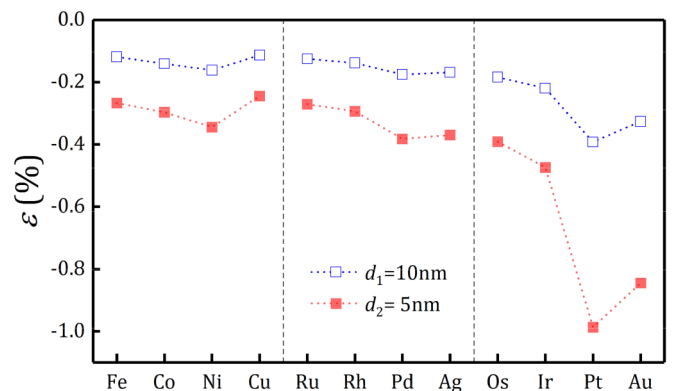


FIG. 3. The internal strain of the transition-metal nanoparticles with the size of 10 nm (open squares) and 5 nm (solid squares), respectively.

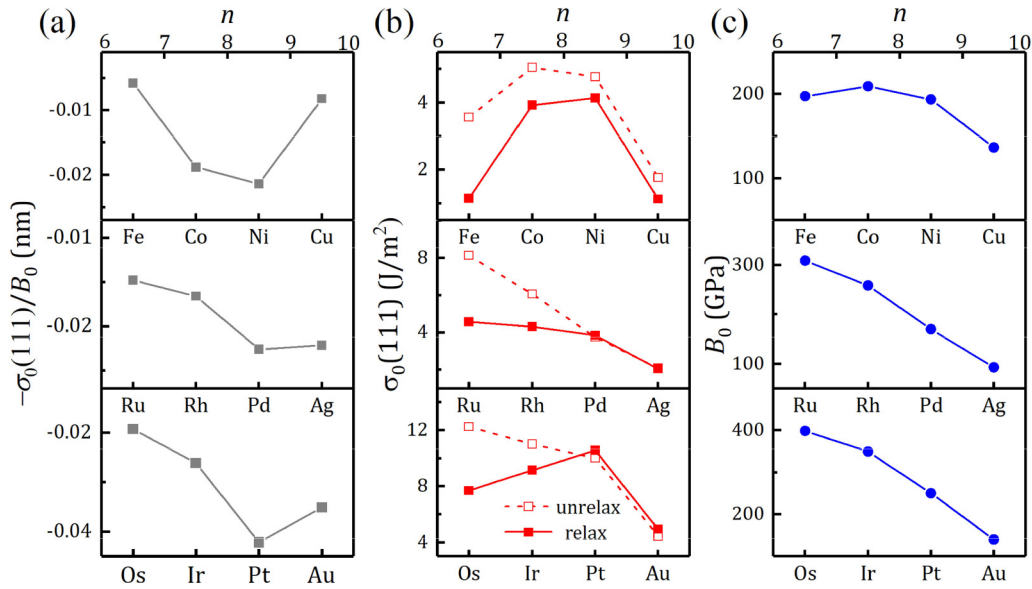


FIG. 4. (a) The negative ratio of surface stress to bulk modulus $-\sigma_0(111)/B_0$, (b) the surface stress $\sigma_0(111)$, and (c) the bulk modulus B_0 as a function of the number of d electrons.

As shown in Fig. 4(a), Ni, Pd, and Pt lie on the lowest points in each period, inconsistent with what shown in Fig. 3. It indicates that the simplification from Eqs. (3) to (4) is reasonable, and the ratio of $\frac{\sigma_0(111)}{B_0}$ plays key roles in determining the internal strain.

Therefore, the phenomenon that the magnitudes of the internal strain of Ni, Pd, and Pt are the largest can be understood from the intrinsic variation of B_0 and σ_0 of the transition metals. According to the Friedel model [43,44], the curve of bulk cohesive energies or unrelaxed surface energies of both $4d$ and $5d$ metals with n looks like a parabola with an opening downward, where n is the number of d electrons ranging from 1 to 10 [45]. The modified Friedel model gives a M -like shape for $3d$ metals varying with n due to the spin polarization [46]. Variations of the bulk modulus B_0 and the surface stress σ_0 of the unrelaxed surface with n also follow the same trends, i.e., in the n -like shape for $4d$ and $5d$ metals and the M -like shape for $3d$ metals. For the considered fcc metals in this paper, the number of the d electrons is $n > 5$. Thus, only the right half of the M -like curve ($3d$) or n -like curve ($4d$ and $5d$) appears as shown by the dashed curves for the unrelaxed σ_0 and the solid curves for B_0 in Figs. 4(b) and 4(c), respectively.

The surface stress σ_0 can be further affected by the surface relaxation. For most of the transition metal the topmost layer tends to relax inward, whereas for some noble metals the outward relaxation occurs [47–50]. As only the inward relaxation favors a smaller surface stress [51], there is a large difference for different metals in the change in surface stress before and after the surface relaxation. As shown by comparison between the dashed curves and the solid ones in Fig. 4(b), the surface stress decreases obviously for $n < 8$. However, for metals with more d -band filling, for instance, Ni/Pd/Pt and Cu/Ag/Au, the surface stress changes little. In fact, we note that the surface stress of Pd(111), Pt(111), and Au(111) even increases after surface relaxation in Fig. 4(b). Considering that both σ_0 and B_0 are concave downward with the change in n , the largest ratio σ_0/B_0 occurs more likely at n of $8 \sim 9$, i.e.,

the group of Ni/Pd/Pt. It indicates that internal strain of a metal nanoparticle eventually depends on the d -band filling for transition metals.

Another feature shown in Fig. 1 is that with the exception of Sr, all the fcc metals exhibit a negative internal strain, which means that a fcc metal nanoparticle usually tends to contract. The negative internal strain of nanoparticles suggests that most of the surfaces are dominated by the positive surface stress. Among the considered metals, however, the metal Sr shows a positive internal strain. Since both Ca and Sr have two s -valence electrons in order to understand the abnormality of Sr, we compare the variations of (111) and (100) surface energy of Ca and Sr with externally applied biaxial strain in Fig. 5. The (110) surface is omitted since its proportion is relatively small, as shown in Table II. We find that the (100) surfaces of Ca and Sr have positive surface stress, just like the other normal fcc metals. However, both (111) surfaces have negative surface stress, consistent with what reported is in

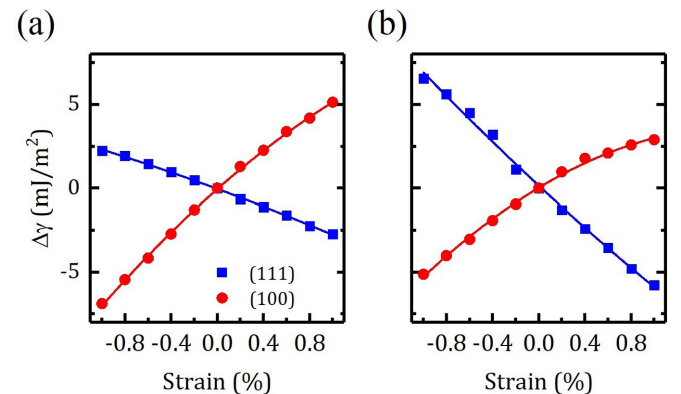


FIG. 5. The change in the surface energies of (111) (solid squares) and (100) (solid circles) of Ca (a) and Sr (b) crystals under the externally applied biaxial strain. The solid lines are the fitting curves according to Eq. (2).

TABLE II. The surface energy γ of three low-index surfaces and their area percentage A (%). γ_a (J/m^2) is the data of the current paper and γ_b (J/m^2) is reproduced from Ref. [33].

Metal	Ca			Sr		
	(111)	(100)	(110)	(111)	(100)	(110)
Surface i	(111)	(100)	(110)	(111)	(100)	(110)
γ_a (J/m^2)	0.47	0.45	0.53	0.34	0.35	0.41
γ_b (J/m^2)	0.46	0.46	0.54	0.35	0.34	0.41
A (%)	44	44	12	62	36	2

Ref. [52] with a larger magnitude for Sr(111) than Ca(111). Furthermore, the total surface area occupied by the (111) plane of Sr is 62%, larger than the corresponding value of Ca as shown in Table II. Thus, the negative surface stress of Ca(111) is compensated by the positive surface stress of the Ca(100) surface, which makes the Ca nanoparticle show a normal negative internal strain. In contrast, the Sr nanoparticle is dominated by the (111) surface due to its higher ratio, showing the abnormal positive internal strain, i.e., lattice expansion. This difference between Ca and Sr comes from the larger surface anisotropy of Sr than Ca because of its larger atomic number.

Negative surface stress is unusual in metals, but it is relatively more common in semiconductors. The abnormality of Sr can partly be explained by its special band structure which suggests that Sr is a semimetal, and even a small gap can be opened up by the spin-orbit interaction [53].

IV. CONCLUSION

To summarize, based on the density functional theory, the bulk and surface elastic properties of fcc metals in plus of the surface energies of all the fcc metals are calculated. According

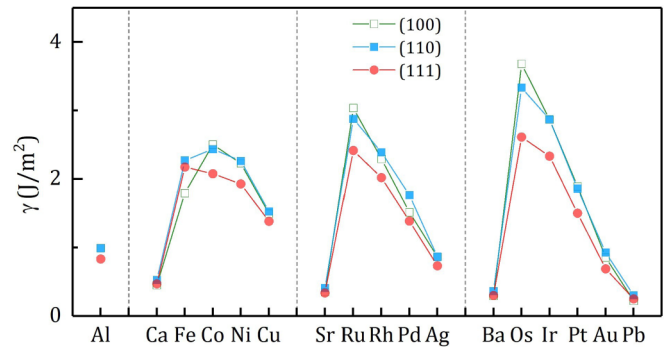


FIG. 6. The surface energies of (100), (110), and (111) surfaces of the fcc metals after the surface relaxation.

to the orientation-dependent surface energies, the stable morphologies of nanoparticles are obtained and are used to study the internal strain as a function of the size. We found that our theoretical results are consistent with the previously reported experimental ones within a wide range of nanoparticle sizes. We also demonstrate that the largest internal strain of the fcc transition-metal nanoparticle larger than 5 nm occurs in the last column of Group VIII (Ni/Pd/Pt), and the fcc metal nanoparticles tend to contract with decreasing size with the only exception of Sr. These findings would help the community to understand the rules and the mechanism of the internal strain of fcc metal nanoparticles.

ACKNOWLEDGMENTS

The numerical calculations were carried out at the High Performance Computing Center of Nanjing University. This work was supported by the National Natural Science Foundation of China (Grants No. 11974164 and No. 12274211).

TABLE III. The comparison of surface energies between this paper and references.

Period	Element	This paper (J/m^2)			Other theoretical simulation (J/m^2)			Experimental value (J/m^2)
		$\gamma(100)$	$\gamma(110)$	$\gamma(111)$	$\gamma(100)$	$\gamma(110)$	$\gamma(111)$	
3	Al	0.99	0.99	0.83	0.91	0.98	0.77	1.16 ^b /0.98 ^c
4	Ca	0.45	0.53	0.47	0.46	0.54	0.46	0.49 ^b
	Fe	1.79	2.27	2.17	2.133 ^a	2.255 ^a	2.077 ^a	1.95 ^c
	Co	2.50	2.44	2.08	2.48	2.42	2.04	3.0 ^d
	Ni	2.23	2.27	1.93	2.21	2.29	1.92	2.45 ^b /2.28 ^c
	Cu	1.50	1.53	1.38	1.47	1.56	1.34	1.825 ^b /1.725 ^c
5	Sr	0.35	0.41	0.34	0.34	0.41	0.35	0.41 ^b
	Ru	3.04	2.88	2.42	2.98	2.81	2.39	hcp 3.05 ^b
	Rh	2.30	2.39	2.02	2.35	2.33	1.98	2.7 ^b
	Pd	1.52	1.77	1.39	1.52	1.57	1.36	2.05 ^b
	Ag	0.87	0.87	0.73	0.82	0.87	0.76	1.25 ^b /1.14 ^c
6	Ba	0.29	0.37	0.30	*	*	*	*
	Os	3.68	3.33	2.61	*	*	*	3.45 ^b
	Ir	2.87	2.88	2.33	2.88	2.83	2.36	3.0 ^b
	Pt	1.89	1.86	1.50	1.86	1.87	1.49	2.475 ^b /3.0 ^c
	Au	0.85	0.93	0.69	0.86	0.91	0.71	1.5 ^b /1.485 ^c
	Pb	0.22	0.30	0.25	0.33	0.33	0.26	0.6 ^b

The data of the theoretical simulations without labels are from Ref. [33]; ^aRef. [54]; ^bRef. [55]; ^cRef. [56]; ^dRef. [58].

TABLE IV. The comparison of elastic constants for 17 fcc metals.

Period	Element	This paper (GPa)			Theoretical work ^a (GPa)			Experimental work ^b (GPa)		
		C_{11}	C_{12}	C_{44}	C_{11}	C_{12}	C_{44}	C_{11}	C_{12}	C_{44}
3	Al	126	54	32	104	73	32			
	Ca	20	13	13	21	15	14			
	Fe	318	124	182	-4	262	28			
4	Co	288	162	146	289	173	148			
	Ni	263	151	128	276	159	132			
	Cu	179	111	80	180	127	78	176	125	82
	Sr	12	8	9	15	10	12			
	Ru	482	222	261	476	226	243			
5	Rh	414	181	187	397	182	177	413	194	*
	Pd	199	148	71	187	147	71	234	176	72
	Ag	130	73	52	100	82	41			
	Ba	10	8	10	*	*	*			
6	Os	595	300	281	579	323	342			
	Ir	581	230	252	576	231	252	600	256	268
	Pt	299	226	58	303	220	54	358	254	77
	Au	165	127	40	144	134	29	202	170	45
	Pb	39	41	6	47	32	18			

^aRef. [59]; ^bRef. [60].

APPENDIX A: GEOMETRY OF NANOPARTICLES

In Eq. (3), B_0 , σ_0 , and S_0 can be directly obtained from DFT calculations. A_i , n_i , and V_0 are determined by the morphology of the nanoparticles constructed according to the Wulff rule. Let us take the distance from the geometric center of a nanoparticle to the exposed (111) surface as h_1 , to the exposed (100) surface as h_2 , and to the exposed (110) surface as h_3 . For convenience $2h_2$ is denoted as d .

(1) The 26-facet nanoparticle:

$$V_0 = 4\sqrt{3}h_1^3 + 4h_2^3 + 16\sqrt{2}h_3^3 + 48\sqrt{6}h_1h_2h_3 - 12\sqrt{3}h_1h_2^2 - 36h_1^2h_2 - 24\sqrt{3}h_1h_3^2 - 48h_2h_3^2.$$

$$A_{100} = -6h_1^2 + 2h_2^2 - 8h_3^2 - 4\sqrt{3}h_1h_2 + 8\sqrt{6}h_1h_3.$$

$$A_{110} = 4\sqrt{2}h_3^2 + 4\sqrt{6}h_1h_2 - 4\sqrt{3}h_1h_3 - 8h_2h_3.$$

$$A_{111} = \frac{3\sqrt{3}}{2}h_1^2 - \frac{3\sqrt{3}}{2}h_2^2 - 3\sqrt{3}h_3^2 - 9h_1h_2 + 6\sqrt{6}h_2h_3.$$

$$n_{100} = 6; n_{110} = 12; n_{111} = 8.$$

(2) The 14-facet nanoparticle:

$$V_0 = 4h_2^3 - 8\sqrt{3}h_1^3 - 12\sqrt{3}h_1h_2^2 + 36h_1^2h_2.$$

$$A_{100} = 6h_1^2 + 2h_2^2 - 4\sqrt{3}h_1h_2.$$

$$A_{111} = 9h_1h_2 - 3\sqrt{3}h_1^2 - \frac{3\sqrt{3}}{2}h_2^2.$$

$$n_{100} = 6; n_{111} = 8.$$

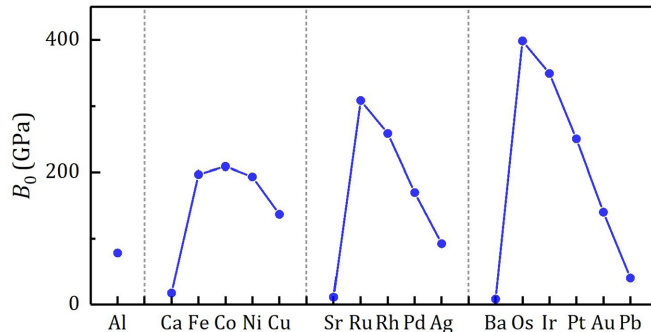


FIG. 7. The bulk modulus B_0 of the fcc metals.

APPENDIX B: THE SURFACE ENERGY

As shown in Fig. 6, the (111) surface always has the lowest surface energy for all these fcc metals. Note that Fe(111) is abnormal partly due to that γ -Fe (fcc) is less stable than the most stable α -Fe (bcc). Actually we find it difficult to reach the convergence during the self-consistent DFT calculations of γ -Fe (fcc). The data of the surface energies are also given in Table III.

APPENDIX C: THE BULK ELASTIC PROPERTIES

The elastic constants of the fcc metals C_{11} , C_{12} , and C_{44} from the DFT calculations are given in Table IV where the referenced theoretical data are reproduced from [57]. The current data are consistent with the previous work [59] with the exception of C_{11} of γ -Fe. It is also worthy to note that for Au, there is about 30% difference between the theoretical value C_{11} (144 GPa) and the experimental value

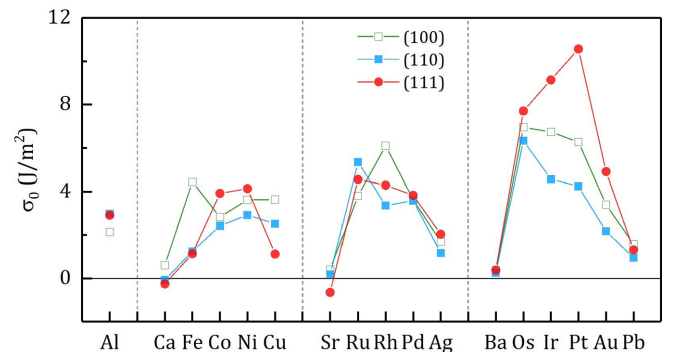
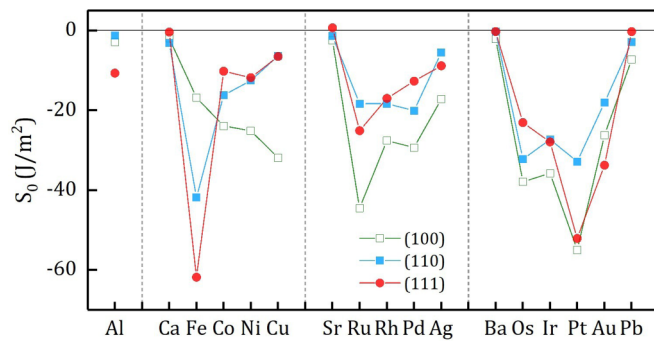


FIG. 8. The surface stress σ_0 of the fcc metals after the surface relaxation.

FIG. 9. The surface elastic constant S_0 .

[60] (202 GPa). In this paper, we use the experimental value to obtain the bulk modulus of Au [61].

The bulk modulus for the fcc crystal $B_0 = \frac{1}{3}(C_{11} + 2C_{12})$ is obtained by using the results shown in Table IV. As shown

in Fig. 7, Ca, Sr, and Ba have smaller B_0 than the transition metals. The bulk moduli of the $4d$ - and $5d$ -fcc transition metals tend to decrease from left to right. Among them, the metal Os has the largest B_0 of nearly 400 GPa.

Note that for the magnetic systems Fe, Co, and Ni, the DFT-PBE method also provides elastic properties comparable with the experimental data [62–65]. Spin-orbit coupling (SOC) may renormalize the elastic properties for heavy elements [66,67]. Fortunately, it has negligible impact on the main conclusion in this paper since the bulk moduli of Pt and Au change little after SOC is included [61].

APPENDIX D: THE SURFACE ELASTIC PROPERTIES

The surface elastic properties are calculated according to Eq. (2). The surface stress is shown in Fig. 8 and the surface elastic constants in Fig. 9 for the relaxed surface. The surface elastic constants are obtained by applying various strain of $-1 \sim 1\%$ within the harmonic approximation.

- [1] P. M. Diehm, P. Agoston, and K. Albe, *Chem. Phys. Chem.* **13**, 2443 (2012).
- [2] S. W. Chan and W. X. Wang, *Mater. Chem. Phys.* **273**, 125091 (2021).
- [3] C. W. Mays, J. S. Vermaak, and Kuhlmann D, *Surf. Sci.* **12**, 134 (1968).
- [4] H. J. Wasserman and J. S. Vermaak, *Surf. Sci.* **22**, 164 (1970).
- [5] H. J. Wasserman and J. S. Vermaak, *Surf. Sci.* **32**, 168 (1972).
- [6] G. Apai, J. F. Hamilton, J. Stohr, and A. Thompson, *Phys. Rev. Lett.* **43**, 165 (1979).
- [7] R. Lamber, S. Wetjen, and N. I. Jaeger, *Phys. Rev. B* **51**, 10968 (1995).
- [8] W. Cai, H. Hofmeister, and M. Dubiel, *Eur. Phys. J. D* **13**, 245 (2001).
- [9] M. Mavrikakis, B. Hammer, and J. K. Nørskov, *Phys. Rev. Lett.* **81**, 2819 (1998).
- [10] B. Hammer and J. K. Nørskov, *Nature (London)* **376**, 238 (1995).
- [11] R. Lazzari, J. Goniakowski, G. Cabailh, R. Cavallotti, N. Trcera, P. Lagarde, and J. Jupille, *Nano Lett.* **16**, 2574 (2016).
- [12] D. Y. Sun and X. G. Gong, *J. Phys.: Condens. Matter* **9**, 10555 (1997).
- [13] J. Woltersdorf, A. S. Nepijko, and E. Pippel, *Surf. Sci.* **106**, 64 (1981).
- [14] D. Nafday, S. Sarkar, P. Ayyub, and T. Saha-Dasgupta, *ACS Nano* **12**, 7246 (2018).
- [15] Q. Jiang, L. H. Liang, and D. S. Zhao, *J. Phys. Chem. B* **105**, 6275 (2001).
- [16] W. H. Qi and M. P. Wang, *J. Nanopart. Res.* **7**, 51 (2005).
- [17] X. H. Yu, J. Rong, Z. L. Zhan, Z. Liu, and J. X. Liu, *Mater. Des.* **83**, 159 (2015).
- [18] Y. X. Xie, J. J. Li, Z. L. Peng, Y. Yao, and S. H. Chen, *Mater. Today Commun.* **24**, 100948 (2020).
- [19] V. B. Shenoy, *Phys. Rev. B* **71**, 094104 (2005).
- [20] S. L. Altmann, C. A. Coulson, and W. Hume-Rothery, *Proc. R. Soc. Lond. A* **240**, 145 (1957).
- [21] G. Grimvall, B. Magyari-Kope, V. Ozolins, and K. A. Persson, *Rev. Mod. Phys.* **84**, 945 (2012).
- [22] J. Häglund, A. Fernández Guillermet, G. Grimvall, and M. Körling, *Phys. Rev. B* **48**, 11685 (1993).
- [23] G. Kresse and J. Hafner, *Phys. Rev. B* **47**, 558 (1993).
- [24] G. Kresse and J. Furthmüller, *Phys. Rev. B* **54**, 11169 (1996).
- [25] M. C. Payne, M. P. Teter, D. C. Allan, T. A. Arias, and J. D. Joannopoulos, *Rev. Mod. Phys.* **64**, 1045 (1992).
- [26] P. E. Blochl, *Phys. Rev. B* **50**, 17953 (1994).
- [27] G. Kresse and D. Joubert, *Phys. Rev. B* **59**, 1758 (1999).
- [28] J. P. Perdew, K. Burke, and M. Ernzerhof, *Phys. Rev. Lett.* **77**, 3865 (1996).
- [29] R. Hill, *Proc. Phys. Soc., London, Sect. A* **65**, 349 (1952).
- [30] J. F. Nye, *Physical Properties of Crystals* (Clarendon Press, Oxford, 1985).
- [31] L. Jia, D. J. Shu, and M. Wang, *Phys. Rev. Lett.* **109**, 156104 (2012).
- [32] I. V. Markov, *Crystal Growth For Beginners*, 2nd ed. (World Scientific, Singapore, 2003).
- [33] R. Tran, Z. H. Xu, B. Radhakrishnan, D. Winston, W. H. Sun, K. A. Persson, and S. P. Ong, *Sci. Data* **3**, 160080 (2016).
- [34] Y. Feruz and D. Mordehai, *Acta Mater.* **103**, 433 (2016).
- [35] Y. G. Sun and Y. N. Xia, *Science* **298**, 2176 (2002).
- [36] K. Sadaiyandi, *Mater. Chem. Phys.* **115**, 703 (2009).
- [37] B. Medasani and I. Vasiliev, *Surf. Sci.* **603**, 2042 (2009).
- [38] B. Medasani, Y. H. Park, and I. Vasiliev, *Phys. Rev. B* **75**, 235436 (2007).
- [39] H. Müller, C. Opitz, K. Strickert, and L. Skala, *Z. Phys. Chem.* **2680**, 625 (1987).
- [40] B. Farkas and N. H. de Leeuw, *Nanotechnology* **31**, 195711 (2020).
- [41] F. Baletto, R. Ferrando, A. Fortunelli, F. Montalenti, and C. Mottet, *J. Chem. Phys.* **116**, 3856 (2002).
- [42] C. H. Chien, E. Blaisten-Barojas, and M. R. Pederson, *J. Chem. Phys.* **112**, 2301 (2000).
- [43] J. Friedel, *Ann. Phys. (NY)* **1**, 257 (1976).
- [44] J. Friedel, *Physica B+C* **109-110**, 1421 (1982).

- [45] M. Nastar and F. Willaime, *Phys. Rev. B* **51**, 6896 (1995).
- [46] M. Alden, H. L. Skriver, S. Mirbt, and B. Johansson, *Phys. Rev. Lett.* **69**, 2296 (1992).
- [47] D. L. Adams, H. B. Nielsen, and M. A. VanHove, *Phys. Rev. B* **20**, 4789 (1979).
- [48] L. D. Marks and D. J. Smith, *Surf. Sci.* **143**, 495 (1984).
- [49] L. D. Marks, V. Heine, and D. J. Smith, *Phys. Rev. Lett.* **52**, 656 (1984).
- [50] S. K. Kwon, Z. Nabi, K. Kadas, L. Vitos, J. Kollar, B. Johansson, and R. Ahuja, *Phys. Rev. B* **72**, 235423 (2005).
- [51] K. Kadas, Z. Nabi, S. K. Kwon, L. Vitos, R. Ahuja, B. Johansson, and J. Kollar, *Surf. Sci.* **600**, 395 (2006).
- [52] J. Y. Lee, M. P. J. Punkkinen, S. Schonecker, Z. Nabi, K. Kadas, V. Zolyomi, Y. M. Koo, Q. M. Hu, R. Ahuja, B. Johansson, J. Kollar, L. Vitos, and S. K. Kwon, *Surf. Sci.* **674**, 51 (2018).
- [53] M. Chellathurai, G. K. Gogovi, and D. A. Papaconstantopoulos, *Materialia* **14**, 100915 (2020).
- [54] J. Yu, X. Lin, J. J. Wang, J. Chen, and W. D. Huang, *Appl. Surf. Sci.* **255**, 9032 (2009).
- [55] F. R. de Boer, R. Boom, W. C. M. Mattens, A. R. Miedema, and A. K. Niessen, *Cohesion in Metals Transition Metal Alloys* (Elsevier Science, The Netherlands, 1988).
- [56] P. M. Anderson, J. P. Hirth, and J. Lothe, *Theory of Dislocation*, 3rd ed. (Cambridge University Press, Cambridge, UK, 2017).
- [57] <https://materialsproject.org/>.
- [58] S. N. Zhevnenko and S. V. Chernyshikhin, *Mater. Lett.* **258**, 126800 (2020).
- [59] M. de Jong, W. Chen, T. Angsten, A. Jain, R. Notestine, A. Gamst, M. Sluiter, C. Krishna Ande, S. van der Zwaag, J. J. Plata, C. Toher, S. Curtarolo, G. Ceder, K. A. Persson, and M. Asta, *Sci. Data* **2**, 150009 (2015).
- [60] P. Söderlind, O. Eriksson, J. M. Wills, and A. M. Boring, *Phys. Rev. B* **48**, 5844 (1993).
- [61] C. Bercegeay and S. Bernard, *Phys. Rev. B* **72**, 214101 (2005).
- [62] J. A. Rayne and B. S. Chandrasekhar, *Phys. Rev.* **122**, 1714 (1961).
- [63] V. I. Razumovskiy, A. V. Ruban, and P. A. Korzhavyi, *Phys. Rev. Lett.* **107**, 205504 (2011).
- [64] M. N. Wang, J. Binns, M. E. Donnelly, M. Pena-Alvarez, P. Dalladay-Simpson, and R. T. Howie, *J. Chem. Phys.* **148**, 144310 (2018).
- [65] M. Yamamoto, *Phys. Rev.* **77**, 566 (1950).
- [66] L. E. Diaz-Sanchez, A. H. Romero, M. Cardona, R. K. Kremer, and X. Gonze, *Phys. Rev. Lett.* **99**, 165504 (2007).
- [67] S. Singh, I. Valencia-Jaime, O. Pavlic, and A. H. Romero, *Phys. Rev. B* **97**, 054108 (2018).